

Small Strain Stiffness: A Micromechanical Experimental Study

J. C. Santamarina

Professor, Georgia Institute of Technology, Atlanta, GA 30332

M. Aloufi

AWOL, Saudi Arabia - Formerly graduate student at U. Waterloo

ABSTRACT: The small strain stiffness of soils is studied with experimental micro-mechanical models designed to separate the relative contributions of different internal processes. The role of particle stiffness and contact behavior, fabric and fabric changes, and normal and tangential interparticle forces is elucidated. It is shown that the exponent of stiffness-stress power relations captures contact behavior if no fabric change takes place, otherwise, the exponent also captures the changes in coordination that occurs during fabric changes. The low-pass filtering effect of particulate media is confirmed in all tests.

1 INTRODUCTION: SMALL&LARGE STRAINS

The variation of the small strain stiffness with stress is captured with power laws, $E=(\alpha\sigma^\beta)^2$. Therefore, a power law also applies to wave propagation velocity vs. stress, but with half the exponent, $V=\alpha\sigma^\beta$. Extensive experimental evidence and analytical studies support the choice of this function. However, the physical meaning of the coefficients remains elusive. Theoretical values for the exponent β are:

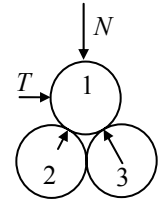
- 0 for an ideal solid
- ~ 0 for a cemented soil (below the transition stress)
- 1/6 for Hertzian contact (elastic spherical particles)
- 1/4 for cone-to-plane contacts
- 3/4 for contacts governed by Coulombian forces
- variable with interparticle distance for contacts varying with electrical DLVO forces

The measurement of small strain parameters (stiffness, Poisson's ratio, attenuation, etc.) is implemented with small perturbations causing strains lower than the threshold strain; in this case, the mechanical response is controlled by contact effects. When the strain exceeds γ_{thres} , the load deformation is governed by other mechanisms such as particle rolling, contact slippage, and fabric changes.

At the micro-scale, the threshold strain can be estimated using Hertzian contacts. Consider a

triangular arrangement of three particles loaded with a normal force N . A shear force T is applied until one of the contacts is lost (sketch below): the 1-3 contact compresses while the 1-2 contact expands until detachment takes place. The lateral displacement of the center of the particle is used to compute the equivalent shear strain:

$$\gamma_{thres} = 1.4 \left(\frac{\sigma}{G} \right)^{2/3}$$



where σ is the isotropic confinement and G is the shear modulus of the material particles are made of.

The strain level plays a subtle and often confusing effect. "Small strain stiffness" measurements do not cause fabric changes, therefore, this is a measure of state. However, velocity-stress relations are determined by wave measurements at different stress states, and the change from one state of stress to another involves fabric changes. Therefore, the velocity-stress power relation captures not only contact behavior but fabric changes as well. In fact, both contacts and contact forces change during loading, in response to the applied boundary conditions.

The evolution of internal microscale parameters is sketched in Figure 1 (numerical simulation results can be found in Rothenburg and Bathurst, 1989). It is important to notice that soils reach limiting

internal anisotropy, in other words, there is a minimum number of lateral contacts (and amount of force) required to prevent the buckling of vertical columns of particles.

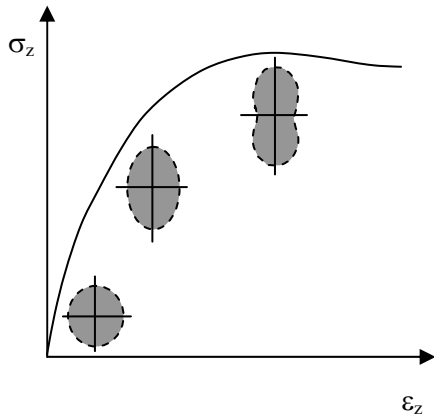


Figure 1. Evolution of internal microscale parameters during deviatoric loading. The sketched polar diagrams represent either the histogram of particle contacts or the average normal contact forces. The polar diagram for average shear contact force resembles 4 leaves aligned with the 45 degree diagonals; the amount of contact shear increases towards the peak strength.

It is also possible to measure a "medium-strain deformation modulus" at each stress state. In this case, fabric changes will develop when one stress state is changed to the next, as well as during the measurement itself. The exponent in the resulting stiffness-stress power relation approaches 1.0 as the strain level increases.

In this paper we present experimental data to elucidate the effect of contact phenomena and fabric changes on low strain stiffness measured with small-perturbation wave propagation techniques.

2 CONTINUUM VS. DISCRETE (Design of Micromechanical Experiments)

The dynamic problem of wave propagation in soils is often approached from the equivalent continuum perspective. This approach is correct as long as the wavelength λ is much greater than the internal scale of the medium "a" (the internal scale is herein assumed to be the particle diameter; however, there are multiple internal scales including conglomerates and layers). Indeed, wave propagation is affected by the discrete nature of soils as the wavelength approaches the particle diameter. When the wavelength is about twice the characteristic spacing,

$\lambda = 2a$, the restitution force between contiguous particles is maximum, the group velocity is $V_g = 0$, and there is infinite attenuation. The variation of the group with the ratio between the wavelength and the particle size λ/a is (Brillouin, 1946; Omar, 1975),

$$V_g = V_\infty \cos\left(\pi \frac{a}{\lambda}\right)$$

where V_∞ is the wave velocity when $\lambda \gg a$. Therefore, the network acts as a low pass filter, and it only transmits waves with $\lambda > 2a$. This observation constrains the design of microscale experiments. On the one hand, one would like to control the internal structure, particle-by-particle. On the other hand, a minimum number of elements is needed to obtain data relevant to the equivalent continuum. In general, a compromise of at least 10 elements in each direction is needed. This renders 3D micromechanical models with a minimum of 1000 particles.

3 THE EFFECT OF STRESS ANISOTROPY (At Constant Fabric)

The study of stiffness changes with stress in particulate media at constant fabric appears not possible in light of Figure 1. To circumvent this restriction inherent to particulate media, an altered two-dimensional analog is built. The frame is 864 x 864 mm. Neoprene strips (0.79 mm thick, 12 mm wide; 36 mm spacing between strips) run along the x and y directions; they are fixed at one end and rest on independent rollers at the other side. Individual weights are hung from the free end of each strip. After tensioning, the intersection of strips is fastened to form a connected two-dimensional "discrete medium". Intersections are disconnected to change the load, and reconnected afterwards.

A pulse generator is used to generate the input that is fed to a speaker cone. A light needle couples the cone to the two-dimensional network. The vibration of the network is monitored with non-contacting proximeter sensors. One proximeter is mounted at the source to capture the input signal. The output from the proximometers are digitized and stored with a PC-based oscilloscope. The distance between source and receiver is ~320 mm.

3.1. Single strip

Wave velocity measurements in an isolated strip are presented in Figure 2. The velocity increases with the load following a power relation. The theoretical

solution for a vibrating string with a $1/2$ exponent is also shown.

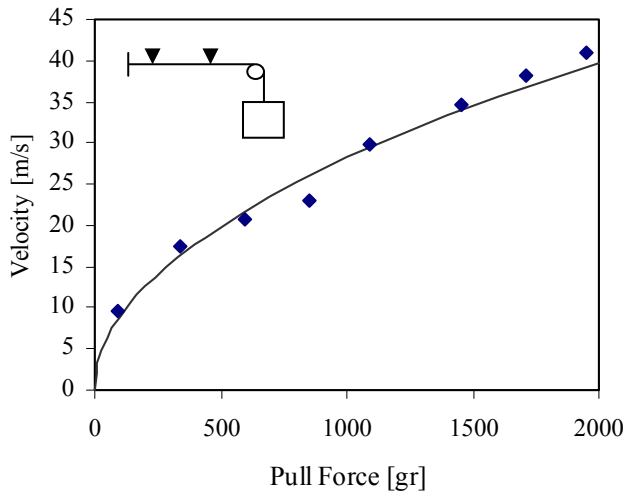


Figure 2. Velocity-Force relation for a single strip. Data and fitted analytical solution

3.2. Isotropic: 500 g weight hung from each strip

Wave velocities computed with measured travel times are shown in Figure 3. Results suggest the development of an isotropic circular wave front (distance is the straight distance from the source to the receiver, as in a continuum). The wave velocity is ~ 14 m/s, rather than 20.4 m/s for the single strip. This is in agreement with the ratio between the "linear mass densities": the contribution of transverse strips at every node produces an equivalent mass density for the network $\delta_{\text{network}} = 2 \delta_{\text{string}}$. Therefore, the decrease in velocity should be approximately $\sqrt{2}$.

The peak-to-peak amplitude of first wavelets is highest along the 45° direction. This indicates a complex vibration mode with higher amplitude in this direction (measurements are performed before reflections, therefore, the data show the propagation of a transient rather than the resonant vibration of a membrane).

The frequency response computed between the input and output signals permits identifying the cut-off frequency corresponding to the low-pass filter effect. While the signal at the source contains frequencies up to $f \sim 400$ Hz, the frequency content in received signals is mostly below ~ 190 - 200 Hz. At this frequency, the wavelength is $\lambda \sim 7.3$ cm. As predicted by Brillouin's analysis, the network acts as

a low pass filter as $\lambda \rightarrow 2d$. The cut-off frequency is not sensitive to direction.

Note that first vibration mode of the network (monitored at the center) is ~ 9.0 Hz, so that the frequency in the imposed transients is much higher than the natural frequency of the network.

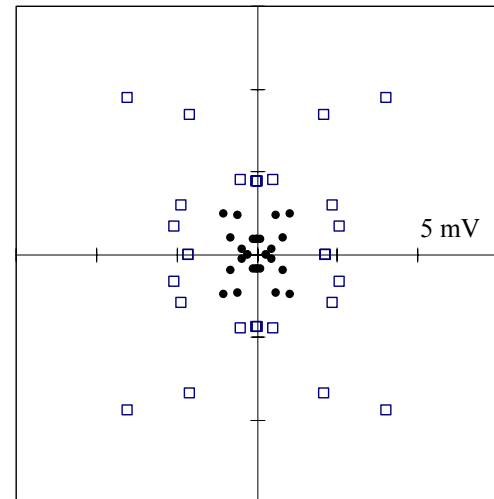
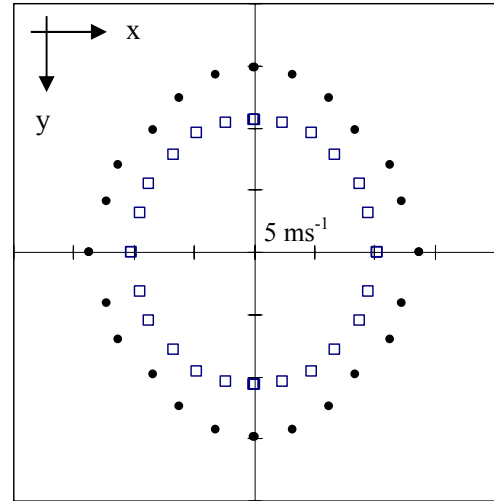


Figure 3. Isotropic loading - Polar plots. (a) Velocity: \bullet first arrival and \square main arrival. (b) Amplitude: \bullet first peak and \square main peak-to-peak

3.3. Anisotropic: 500 g in X and 1000 g in Y

The polar diagram of velocity in Figure 4 shows an elliptical wave front, with elongation in the direction of the higher load. The highest velocity is approximately 20 m/s (the velocity in an isolated strip for 1000 g load was 28.5 m/s - the difference reflects the effect of mass density). The anisotropy in velocity predicted from the anisotropy in forces $(1000/500)^{0.5}$ is about the same to the measured

anisotropy 20/13. The polar diagram for amplitude magnifies the diagonal effect observed in the isotropically loaded network and it is slightly slanted towards σ_1 . A directional analysis of energy and frequency does not add conclusive information. Most of the energy is contained below 200-250 Hz, rendering an average cut-off at $\lambda \approx 2d$.

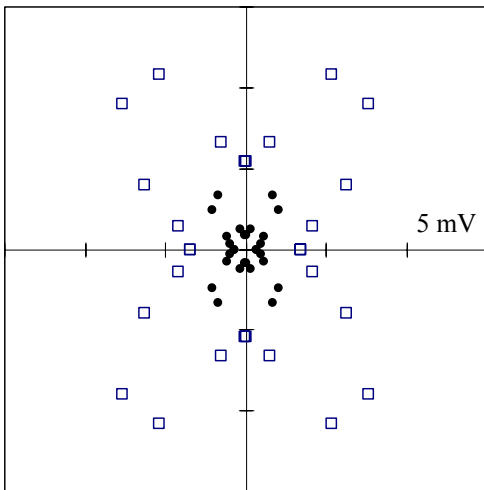
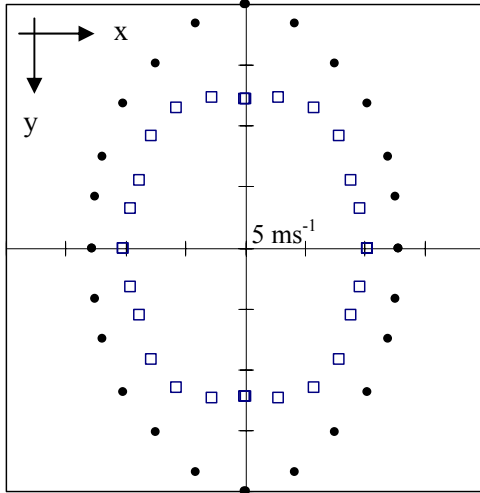


Figure 4. Anisotropic loading - Polar plots. (a) Velocity: • first arrival and □ main arrival. (b) Amplitude: • first peak and □ main peak-to-peak

3.4 Comments

These results show that the evolution of velocity with isotropic and anisotropic stresses at constant fabric can be predicted from the wave propagation characteristics of a single strip, i.e., the prevailing contact behavior. Results also confirm the low-pass filtering effect of particulate materials.

The polar plots can be readily fitted with a Fourier series, $\text{Parameter}(\theta) = A + B\cos 2\theta + C\sin 2\theta + D\cos 4\theta + E\sin 4\theta + \dots$. Velocity plots show that

anisotropy can be captured with first and second order terms. On the other hand, fitting the amplitude plots requires the fourth order terms.

4 ELASTIC-PLASTIC CONTACT BEHAVIOR (Constant Fabric)

A one-dimensional packing of spheres is tested to provide information on the velocity stress exponent in the transition from elastic to plastic contact behavior at constant fabric. The stiffness of a Hertzian contact can be either related to the applied force or to the size of the contact area. The second alternative permits computing the *small strain stiffness* of a particulate matrix if the area of contacts is known, regardless of the mechanisms that caused the flattening of the contact (elastic, viscous or plastic behavior).

In particular, it can be shown that the small-strain stiffness relates to the state of stress to a power 1/2 when contact yield takes place, therefore (Cascante and Santamarina, 1996),

$$V = \alpha \cdot \sigma^{1/4}$$

This is experimentally assessed with a 15-particle column constrained from buckling by means of individual rings around each particle (internal diameter of rings: 25.58 mm; diameter of polypropylene particles: 25.33 mm). Rings are carefully aligned and held in position within an external Plexiglas cylinder (380 mm high - three millimetric screws position each ring). The double ring-cylinder support system avoids wave transmission along the support.

The normal load is applied onto the end-particles. Piezocrystals transducers placed between the loading platens and the end-particles act as source and receiver. Received signals are digitized, stored and post-processed. This device allows the study of P-wave propagation in aligned spherical particles during loading and unloading.

Figure 5 shows the results obtained with this 1D arrangement. The equivalent vertical stress is computed dividing the applied load by the square of the diameter of particles. Two regions are apparent. They are characterized by linear segments in the log-log plot. The Hertzian model fits the first region, i.e., exponent $\beta = 1/6$, with $\alpha = 254$ m/s. The second region is fitted with the exponent corresponding to contact yield, $\beta \approx 1/4$. The transition from the elastic to the plastic regime takes place at around $\sigma \approx 100$ kPa.

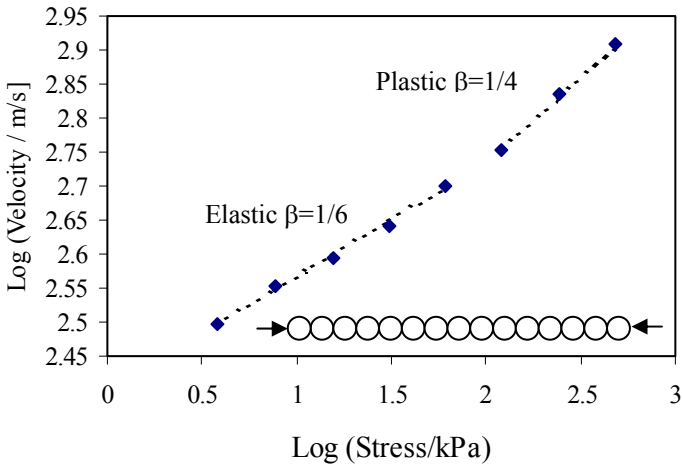


Figure 5. Elasto-plastic contact behavior in spherical particles

5 THE EFFECT OF FABRIC CHANGES (SC Packing in a 3D True Triaxial)

Small strain wave propagation in particulate materials subjected to fabric changes is studied with micro-mechanical experiments conducted within a true triaxial, using the same particles as in the previous study. Three walls are aluminum plates, while the other three are rigid Plexiglas plates to permit observing the packing at all stages. The aluminum walls are covered with a 1.5 mm thick neoprene membrane to reduce the effect of small imperfections. Wave measurements are conducted at the middle plane using thin piezocrystal pads.

The simple cubic packing SC is formed within the true triaxial device by placing rows and columns parallel to the boundary walls. A total of 12 particles are placed in each direction. Altogether, this packing includes 1728 particles. The initial adjustment of the walls is done in the x and y directions to guarantee contacts among particles in all directions. The vertical gravity load in the z direction is applied at no lateral strain ($\epsilon_x = \epsilon_y = 0$). Then, lateral relaxation is enforced along the x direction causing contact loss in direction- x (at $\epsilon_y = 0$). The subsequent loading history consists of (1) lateral re-loading in the x direction maintaining constant the vertical load and $\epsilon_y = 0$, and (2) lateral unloading in the x direction under the same conditions.

Note that the simple cubic packing has the minimum coordination number for a stable arrangement of frictionless particles. During relaxation, the average coordination number drops slightly below 6 (assuming 1 contact lost per row, the average coordination number becomes 5.92; therefore, shear must be mobilized at contacts). Vertical columns buckle, and the packing becomes

rearranged in zigzag patterns along vertical columns (in fact, forces against horizontal boundaries increase for large lateral relaxations). During reloading, a maximum stress ratio of 9.4 is reached in the xz plane. However, the stress ratio remains very low in the yz plane. Hence, the load in x has virtually no effect on the state of the stress in the y direction under constant vertical stress σ_z . The nature of the simple cubic packing readily explains this observation: a limiting 0-force is required in y to maintain the alignment of particles along rows.

Velocity. In agreement with the fairly inactive stress history along the y direction, the velocity in y , V_y , remained unaltered throughout the loading history. On the other hand, the velocity in the z direction V_z shows changes above the noise-level; as the vertical load remains constant; these changes reflect changes in low stiffness primarily due to alterations in fabric. Obviously, the most significant changes in velocity occurred in the x direction, V_x (Figure 6). Results are shown in log-log scale to highlight different power trends. As the relaxed packing is laterally reloaded, the velocity V_x increases at a low rate, resulting in a exponent $\beta = 0.04$. In the transition region, changes in contact behavior and changes in fabric cause the exponent to reach $\beta = 0.31$ (see Goddard, 1990). During final lateral unloading, the velocity decays at a Hertzian rate, $\beta \approx 1/6$, until the fabric breaks down with column buckling ($\beta=0.10$). The 3 stages identified in the velocity stress plot $V_x - \sigma_x$, are also observed in the stress-strain history.

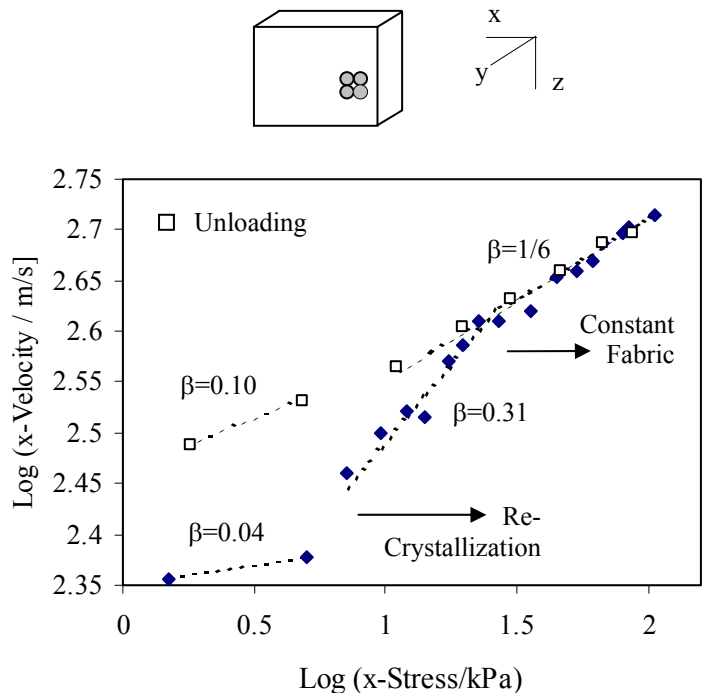


Figure 6. Velocity stress relation. The effect of fabric changes (change in particle coordination)

Frequency Content. A summary of cut-off frequencies versus the stress history is shown in Figure 7. Clearly, changes in frequency agree with changes in fabric (albeit at a shifted stress level), also detected in velocity measurements. The wavelength corresponding to 2000 Hz is about $\lambda=20$ cm, which is about 8 particle diameters. This is greater than Brillouin's cut-off frequency ($\lambda = 2$ diameters). A careful look at the power spectral density of the output signals shows that higher frequencies are present, often reaching 4000 Hz in the re-crystallized packing. However, the amplitude of those high frequency components is significantly lower than the amplitude selected to identify the cut-off frequencies reported in Figure 7.

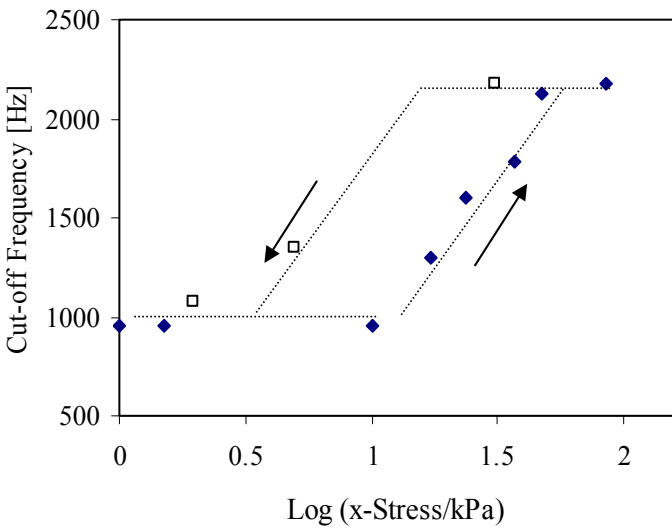


Figure 7. Evolution of cut-off frequency during changes in coordination

Attenuation. The evaluation of energy losses is not possible in this 3D geometry due to spreading. Furthermore, the performance of piezocrystal pads is dependent on the contact force. The only salient feature in the evolution of the amplitude of received signals is a clear increase at around $\sigma_x \approx 18$ kPa that corresponds to the center of the transition region.

6 PARTICLE ARRANGEMENT

The α Coefficient and Poisson's Ratio

The monitoring of wave propagation parameters during stress and fabric changes has also been extended to the cubic tetrahedral and the face-centered cubic packing. These are assembled in the same triaxial device and subjected to similar load-

deformation histories. Overall trends are similar to those observed in the simple cubic packing, yet, several relevant features can be identified. A summary of main observations is presented in Table 1 (Note: the stiffness of regular packings is anisotropic).

The α -coefficient predicted for a simple cubic packing and Hertzian contact is

$$\alpha = 3 \sqrt{\frac{[kPa]}{\pi \cdot \rho_{part}}} \cdot \left[\frac{2 (G/[kPa])}{3 (1-\nu)} \right]^{1/3}$$

Measured alpha-values for the tree packings are different. Based on these and previous results, the coefficient alpha depends on the material of the particle, the type of contact, and the packing.

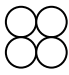
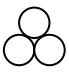
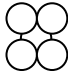
The value of *large-strain Poisson's ratio* in the xz plane is determined based on deformations measured during reloading. Values are also predicted based on the kinematics of rigid particles, by means of simple trigonometric analyses. Measured and predicted values are in close agreement (see Table 1). On the other hand, wave propagation causes deformation primarily at contacts; this renders very small values of *small strain Poisson's ratio*, in general $\nu \leq 0.1$ and in particular $\nu=0$ for SC packing (Santamarina and Cascante, 1996).

7 NORMAL AND SHEAR CONTACT FORCES

The CT packing shows higher velocity than the FCC packing, even though the coordination number of CT is only 8 as compared with the coordination of 12 corresponding to FCC. One explanation relates to the testing direction relative to the crystal directions. As indicated in Table 1, should all the x-force be transmitted along the chains of particles that contact the boundaries, the CT packing would carry a higher force per chain than the FCC, suggesting flatter contacts and higher stiffness, in agreement with measurements.

Another effect relates to the role of shear forces mobilized at contacts in the different packings. Consider the simple cubic packing. The evolution of contact forces is qualitatively studied with photoelastic disks. The loading history resembles the one imposed in the study described above. Results are shown in Figure 8. Figure 8-c highlights the relevance of shear at contacts to the overall stiffness of the packing. Figure 8-d shows that Hertzian row stiffness is crucial to the lateral load-deformation behavior of the re-crystallized packing; however, shear at the contacts still remains and Mindlin-shear

Table 1: Results for Different regular packings - Summary

Packing	SC	CT	FCC
2D Sketch along the zx plane			
Void ratio e	0.476	0.342	0.183
Coordination number	6	8	12
Inter row vertical separation	d	$1.7 d$	$1.4 d$
Number of particles in test	1728	1734	2264
X-stress at end of the transition	18 kPa	13 kPa	36 kPa
Large-strain Poisson's ratio ν_{zx} during transition region: computed ($\varepsilon_x=1/25-1/100$) measured	0.001 - 0.005 0.11	0.29 - 0.3 0.32	0.35 - 0.36 0.32
V_x at $\sigma_x=100$ kPa (re-crystallized)	512 m/s	770 m/s	613 m/s
Force per particle in full rows *	$\sigma_x d^2$	$1.7 \sigma_x d^2$	$1.4 \sigma_x d^2$
Wave parameters $V=\alpha(\sigma/kPa)^\beta$ β in transition region α re-crystallized region β re-crystallized region	0.326 240 m/s ♣ 0.168 ♣	1.007 380 m/s 0.152	0.57 290 m/s 0.171

Notes: * Re-crystallized. It assumes that all the boundary stress is carried as normal force along the rows of particles that contact boundaries (i.e., overwhelming effect of normal force over shear component)
♣ For the 1D arrangement, $\alpha=254$ m/s and $\beta\approx 0.167$

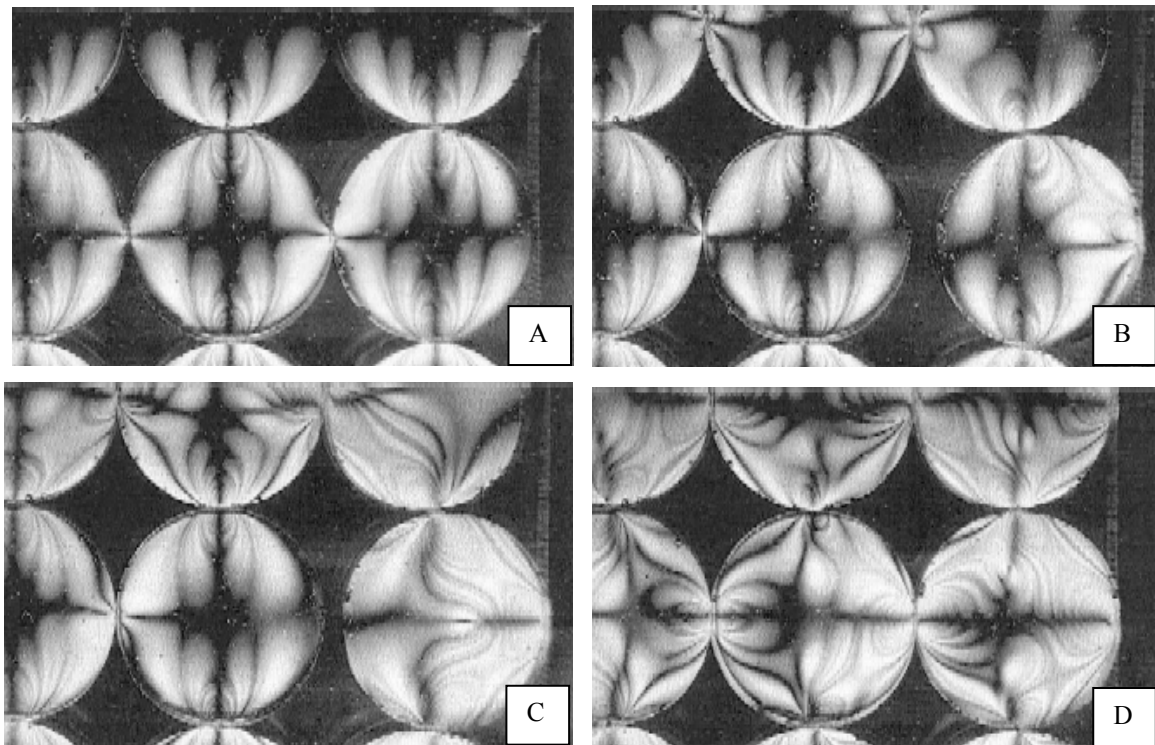


Figure 8. Photoelastic study of changes in contact forces during fabric changes (only 9 disks shown): (a) disks in equivalent simple cubic packing arrangement are vertically loaded; virtually no lateral load is mobilized. (b) Lateral boundaries are moved outwards; the column on the right buckles causing horizontal forces and shear at contacts between disks, as denoted by the rotation of fringes around the contacts. (c) Lateral loading is initiated from the right wall; the boundary disk that buckled is subjected to significant lateral loading which is transmitted by shear to the particles immediately above and below; during loading, slip takes place along these contacts. (d) Upon further horizontal loading, horizontal contacts are regenerated.

stiffness contributes to the overall lateral stiffness of the packing. It is important to note that early studies of regular packings neglected Mindlin stiffness, for simplicity, and predicted lower stiffness of packings (see Deresiewicz, 1974). Duffy and Mindlin (1957) showed that the compressional stiffness of a face centered cubic packing is 1.4 to 1.7 times higher (depending on crystallographic orientation) when shear tangential forces are considered in the analysis. It is important to realize that normal and shear forces at contacts depend on the loading history.

8 CONCLUSIONS

Small strain measurements characterize state, while large strain mechanical measurements reflect changes in state. Therefore, small and large strain parameters respond to different internal mechanisms.

At constant fabric, stiffness-stress data denounces contact phenomena: geometry, elastic-plastic-brittle contact, breakage in cementation and grain crushing, as well as the contribution of normal and shear contact stiffness to global stiffness. However, varying the state of stress affects both fabric and interparticle forces. Thus, stiffness-stress relations capture the combined effects of contact behavior, fabric changes, and the evolution of contact forces.

Discrete media such as soils and fractured rocks are inherently dispersive, low pass filters. Changes in fabric affect the dispersion characteristics.

An exponent β greater than the Herzian exponent $\beta=1/6$ can be due to non-spherical contact, yield or viscous deformation at contacts, increase in coordination, and surface-related electrical forces.

ACKNOWLEDGEMENTS - WEB

Ken Bowman assisted in the design and construction of devices and Teresa Hyungh helped in conducting the 2D tests. Support for this research was provided by the Government of Saudi Arabia and by the US National Science Foundation. Related information can be found in <http://www.ce.gatech.edu/~carlos/>

REFERENCES

Brillouin, L (1946), *Wave Propagation in Periodic Structures*, McGraw-Hill, New York, 247 pages.

Cascante, G. and Santamarina, J.C. (1996), Interparticle Contact Behavior and Wave Propagation, *ASCE Geotechnical Journal*, vol. 122, no. 10, pp. 831-839.

Deresiewicz, H. (1974), Bodies in Contact with Application to Granular media, *R.D. Mindlin and Applied Mechanics*, Ed. G. Herrmann, Pergamon Press, New York.

Dobry, R., Ladd, R.S., Yokel, F.Y., Chung, R.M., and Powell, D. (1982). Prediction of Pore Water Pressure buildup and Liquefaction of Sands During Earthquakes by the Cyclic Strain Method, *Building Science Series 138*, US Dept. Commerce, National Bureau of Standards.

Duffy, J. and Mindlin, R.D. (1957), Stress-Strain Relations of a Granular Medium, *J. Applied Mechanics*, vol. 24, no. 4, pp. 585-593.

Goddard, J.D. (1990), Nonlinear Elasticity and Pressure Dependent Wave Speeds in Granular Media, *Proc. Royal Society of London*, vol. 430, pp. 105-131.

Omar, M.A. (1975), *Elementary Solid State Physics*, Addison Wesley, Reading Ma, 669 pages.

Rothenburg, L. and Bathurst, R.J. (1989), Analytical Study of Induced Anisotropy in Idealized Granular Material, *Geotechnique*, vol. 39, no. 4, pp. 601-614.

Santamarina, J.C. and Cascante, G. (1996), Stress anisotropy and wave propagation -A micromechanical view-, *Canadian Geotechnical Journal*, vol. 33, no. 5, pp 770-782.